Construct 3D Pd@MoS₂-conjugated polypyrrole framworks Heterojunction with unprecedented photocatalytic activity for Tsuji-Trost reaction under visible light

Jian Liu[a,c,1], Xijiao Mu[b,1], Yanmei Yang[a], Fengjuan Chen[a], Jingang Wang[d], Yuee Li[b,*], Baodui Wang[a,*]

[a] State Key Laboratory of Applied Organic Chemistry, Key Laboratory of Nonferrous Metal Chemistry and Resources Utilization of Gansu Province, College of Chemistry and Chemical Engineering, Lanzhou University, Lanzhou, 730000, China
[b] School of Information Science and Engineering, Lanzhou University, Lanzhou 730000, China
[c] Institute of Advanced Materials, College of Chemistry and Chemical Engineering, Jiangxi Normal University, Nanchang, 330022, China
[d] Liaoning Shihua University, Fushun 113001, China

ARTICLE INFO

ABSTRACT

Site-selective coupling of two photochemical system and one electron-transfer system to realize efficient charge separation and light absorption affords a promising route to enhance the photocatalytic efficiencies of semiconductors. To date, however, how to develop 3D porous multicomponent heterojunction systems for solar energy conversion in the visible and near-infrared (NIR) light region still remains a significant challenge. Here we report a simple technique for forming 3D Pd@MoS₂-conjugated polypyrrole framworks (Pd@MoS₂CPFs), in which two visible-light-active components (MoS₂ nanosheets and polypyrrole) and the electron-transfer system (Pd) are spatially fixed, and the uniform Pd NPs are anchored in the MoS₂CPFs. This 3D porous system exhibits good structural stability, high pore volume (0.31 $cm^3 g^{-1}$), high surface area (105.24 m^2/g), improved light absorption, and a long living electron-hole pair at the Pd@MoS₂CPFs interface. Unexpectedly, we first found that the formed Pd@MoS₂CPFs exhibited excellent photocatalytic activity and long-term stability for the direct Tsuji-Trost reaction between allylalcohol and 1,3-dicarbonyl under visible light at room temperature, far exceeding those of the single- and two-component systems, as a result of vectorial electron transfer driven by the one-step excitation of polypyrrole and MoS₂. These results provide a promising new avenue in the design and fabrication of unique 3D porous multicomponent heterojunction for visible-light-induced efficient artificial photosynthetic systems.

1. Introduction

Driven by the limited supply of the current worldwide energy and environmental issues, the efficient use of solar energy has received wide interest [1–6]. Up to date, three primary solar energy technologies including solar heating, solar photovoltaics, and solar thermal electricity have been used for solar-to-electricity conversion and solar water heating [7–9]. Besides these technologies, the use of sunlight to drive chemical reactions has received significant attention for solar conversion to electricity or fuels based on electron/hole pair production in semiconductors [10–13]. Although the fact that great progress has been made, the practical application of photocatalytic technology is still lack of efficient photocatalyst due to low photocatalytic efficiency and limited visible and near-infrared (NIR) photoabsorption [14–16]. Thus, it is still necessary to design novel light-driven photocatalyst systems to improve photocatalytic efficiencies for the requirements of future environmental and energy technologies.

Among the numerous semiconductor based photocatalysts, molybdenum disulphide nanosheets (MoS₂ NSs) have attracted much attention because of their narrow direct band gap of ~1.9 eV, visible-light-harvesting function, and high stability against photocorrosion [17–19]. It is believed that MoS₂ NSs will play an increasingly significant role in the fields of photocatalysis. Nevertheless, it still suffers from some drawbacks, such as restacking of the sheets because of van der Waals forces, small specific surface area, low visible light utilization efficiency, and rapid recombination of photogenerated carriers [20]. To

---

overcome the aforementioned problems, much efforts have recently been devoted to constructing MoS_2 based nanohybrids [21–27]. Among them, MoS_2 matrices with 3D porous structure have attracted increasing attention due to their unique structural characteristic, which afford their stable mechanical, unique chemical and physical properties, and high ratio of surface to volume and high light absorption. As a result, these 3D porous MoS_2 based materials hold great promise for widespread applications involving catalysis, sensor, and energy fields, *etc* [25–27]. To date, most of these MoS_2-based frameworks are fabricated by physical interactions of MoS_2 and other motives building blocks [14,25–27], which results low activity and poor durability. In addition, tremendous efforts have recently been made in developing more abundant visible and NIR-absorbing nanomaterials, which allows for utilization of 43% and 53% of the solar light respectively [28]. However, fabricating MoS_2-based hierarchical structures for photocatalytic activity in visible light that is sufficiently stable and efficient for practical use remains challenging.

Recently, intergating semiconductor nanomaterials with a conducting polymer (CPy) has been shown to be an effective means of promoting charge carrier separation and improving visible-light activity [29,30]. Among other well known π-conjugated conducting polymers, polypyrrole (PPy) has been of particular interest because of its easy preparation, high electrical conductivity and large surface area [31–33]. Moreover, PPy chains containing numerous nitrogen atoms would control growth of metal nanoparticles and benefit efficient coordination with the formed NPs [34,35]. A significant effort has been devoted to create heterojunction materials containing a PPy layer as well as an inorganic layer, and polymer intercalation in MoS_2 sheets, or growth and assembly MoS_2 on multi-dimensional polymers [36–38]. Despite numerous efforts, there is still only limited information on the synthesis of hierarchical MoS_2 frameworks through effective covalent bonds between MoS_2 and PPy.

In addition to the above mentioned approaches, noble metal NPs with localized surface plasmon resonance (LSPR) effect have been shown to be good materials for contributing to enhance the electron-hole separation and interfacial charge transfer [39–42]. However, small noble metals NPs are usually considered a lack of continuous uniform distribution in view of aggregation, which would decrease electron transfer. In addition, direct contact between the metal and the semiconductor may also introduce interface trapping states that can increase electron hole recombination and Fermi level pinning to degrade the photocatalytic activity [33,42]. Generally, coating thin layers of CPy onto noble metals/semiconductor surfaces not only can enhance the conductivity but also can concentrate light for the enhancement of photocatalytic activity [33,42]. Though some recent advances have been made to produce some CPy/noble metal/MoS_2 composite microspheres, the construction of such 3D porous structure has not been explored until now.

On the other hand, the Tsuji–Trost allylation of various nucleophiles is a kind of important reaction to the formation of C−C, C−N, and C−O bonds in the synthesis of biologically important molecules [43]. These reactions are generally catalyzed by Pd catalysts under high temperature, which easily produced some by-products. As photocatalytic reactions are mostly conducted at ambient temperature and atmospheric pressure, many intermediates are stable under such conditions and would not react further [44]. If the Tsuji–Trost reaction can be realized by a photocatalytic process, the synthesis of compounds would be a much more controlled, simplified, and greener process. However, to our best knowledge, there is no report that such reaction could be catalyzed by photocatalyst under the visible light at room temperature.

In this work, we present a universal strategy for the first synthesis of robust 3D conjugated-polypyrrole-frameworks (Pd@MoS_2CPFs) by ultrasound mediated one-step redox/complexation process, in which Pd NPs and PPy layer were inserted between the layers of MoS_2 by reduction of noble-metal salts and polymerization of pyrrole, respectively. In such process, porous 3D frameworks were constructed by

forming amidate between the carboxyl groups on the MoS_2 NSs and amido of PPy as well as the coordination between molybdenum atoms in MoS_2 and nitrogen atoms in PPy. Such a composite structure can embody the advantages of each component: (i) MoS_2 NSs with uniform distribution and high surface area immobilize conducting polymers for the charge storage; (ii) Pd NPs offer an electron transfer expressway to separate electron and hole (e^-/h^+) pairs; (iii) PPy layer not only can enhance the conductivity but also can enhance NIR light absorption to increase more photogenerated e^-/h^+ pairs. To the best of our knowledge, this is the first time that three-component nanostructures with high porosity have been prepared via a facile one-pot synthetic approach. The as-prepared nanohybrids have a well-defined 3D morphology, confined metal NPs in the matrix, high surface area, and enhanced optical absorption capacity, promising candidates as visible light enhanced photocatalysts. With these merits, Pd@MoS_2CPFs hybrid framworks exhibited unexpected photocatalytic activity and robust cycling for the direct Tsuji-Trost reaction between allylalcohol and 1,3-dicarbonyl under visible light at room temperature.

2. Experimental

2.1. Chemicals

All reagents were used without further purification: from Sigma-Aldrich, pyrrole, α-lipoic acid (LA), palladium acetate (Pd(OAc)$_2$, 99%), and ethylene carbonate (EC); from Alfa Aesar, n-butyllithium solution in hexane (1.6 M), molybdenum(IV) sulfide flake (MoS_2, 99%). MoS_2 NSs were synthesized by chemical exfoliation method using similar method according to the literature and dispersed in DMF as stock solution [45].

2.2. Measurements

The morphology of the samples was investigated by field-emission scanning electron microscope (FE-SEM, FEI, Sirion 200) and transmission electron microscope (TEM, JEOL, JEM-2100, 200 kV). X-ray powder diffraction (XRD) patterns of the nanomaterials were recorded on a Bruker AXS D8-Advanced diffractometer with Cu Kα radiation (λ = 1.5418 Å). N$_2$ adsorption-desorption isotherms were measured at 77 K after heating the samples at 120 °C for 8 h to remove any moisture and solvent molecules presented in the pores with Micromeritics TriStar II 3020 analyzer. The Brunauer-Emmett-Teller (BET) method was utilized to calculate the specific surface areas (S_{BET}). By using the Barrett-Joyner-Halenda (BJH) model, the pore volumes and pore size distributions were derived from the adsorption branches of isotherms. X-ray photoelectron spectroscopy (XPS) measurements were performed on a PHI-5702 multifunctional spectrometer using Al Kα radiation. The XPS profiles were fitted by the Gaussian–Lorentzian method after background subtraction using Shirley's method [46]. Raman spectra were collected using a confocal microprobe Raman system (Renishaw, RM2000). FT-IR spectra were recorded on a Nicolet FT-170SX spectrometer. UV–vis–NIR diffuse reflectance spectra were carried out on an Agilent Cary 5000 UV–vis–NIR Spectrophotometer. Pd contents are determined by inductively coupled plasma-atomic emission spectrometry (ICP-AES, Varian VISTA-MPX). Photocalysis was performed using a **white** LED lamp (30 W). ^{1}H-NMR and ^{13}C-NMR spectrums were gathered on a JEOL ESC 400 M instrument.

2.3. Synthesis of MoS$_2$-LA

MoS_2 NSs (250 mg) dispersed in 80 mL DMF by ultrasound, and then LA (21 mg, 0.1 mmol) dissolved in 20 mL DMF was slowly added into the above dispersed solution. After sonicating and stirring overnight, the mixture was added with diethyl ether (40 mL). The formed MoS_2-LA was collected and washed with DMF and diethyl ether for four times and then dispersed in acetonitrile (50 mL).

2.4. Synthesis of Pd@MoS₂CPFs

For the preparation of Pd@MoS₂CPFs nanohybrids, MoS₂-LA (40 mg, 8 mL) solution was diluted in acetonitrile (40 mL) and sonicated for 30 min. Py solution (diluted in acetonitrile at 500 mM, 2 mL) was added and sonicated for another 0.5 h. Then Pd(OAc)₂ solution (dissolved in acetonitrile at 100 mM, 1 mL) was slowly added, and the mixture sonicated for 1 h under 28 ~ 32 °C. The precipitate was collected and washed with acetonitrile and water until effluent became colorless and pH-neutral, followed freezing dry. The composite powder was subjected to heat-treatment at 200 °C for 2 h under Ar. After cooling down to room temperature, some residue was removed by deionized water soak to obtain Pd@MoS₂CPFs.

2.5. Synthesis of MoS₂CPFs, Pd@CPFs and PPy

MoS₂CPFs was synthesized using (NH₄)₂S₂O₈ as initiator in water according to the literature.[22] Briefly, Py (350 μL) was added into MoS₂ suspension (20 mL, 1 mg mL⁻¹) under stirring for 30 min. (NH₄)₂S₂O₈ solution (228 mg, 5 mL) was added dropwise to induce polymerization of pyrrole. The mixture was stirred for 12 h at r.t. The precipitate was collected and washed with acetonitrile and water until effluent became colorless and pH-neutral, followed by freezing dry. The composite powder was subjected to heat-treatment at 200 °C for 2 h under Ar. Pd@CPFs was prepared without adding MoS₂. PPy was synthesized as mentioned above except without adding MoS₂, and replacing Pd(oAc)₂ with (NH₄)₂S₂O₈.

2.6. General procedure for the Pd@MoS₂CPFs nanohybrids catalyzed Tsuji-Trost reaction

For the Tsuji-Trost reaction, 0.5 mmol of 1,3-dicarbonyl, 1.5 mmol of allylalcohol, 1.5 mmol of Cs₂CO₃, 4 mg Pd@MoS₂CPFs catalyst (Pd: 5 μmol), and the mixture solution of H₂O/EC (2.0 mL/0.5 mL) were used. The reaction was carried out in a N₂ covered glass tube under a white LED lamp (30 W) at 25 °C. After the reaction completed, the mixture was diluted with 3 mL of ethyl acetate and washed with water (3 × 3 mL). The products were characterized by MS, ¹H-NMR, and ¹³C-NMR. In order to study the cycle stability of catalyst, the isolated catalyst was activated by acetone and used in the recycling reaction. As a control, the same reaction was conducted in dark condition at room temperature.

2.7. Cyclic voltammetry (CV) analysis

To investigate the redox propertie of PPy, CV analysis was performed with a standard three-electrode system, which consists of an Ag/AgCl reference electrode (0.01 M AgNO₃, 0.1 M TBACMP₆ in CH₃CN), a platinum sheet working electrode and a platinum wire counter electrode. The electrolyte solution employed was 0.10 M TBACMP₆ in freshly dried CH₃CN, and ferrocene/ferrocenium redox coupled (Fc/Fc⁺, −4.8 eV) was used as the reference material for all CV measurements. CV was recorded at 100 mV/s under a N₂ atmosphere.

2.8. Transient photocurrent density measurement

Photoelectrochemical properties were investigated on an electrochemical station (CHI 760E) in a standard three-electrode, single-compartment quartz cell. and the working electrodes with an active area of 2 cm². The counter electrode and reference electrode consisted of a Pt sheet (99.99%, 0.1 mm, 1 cm × 2 cm) and Ag/AgCl, respectively. A 300 W Xe lamp with filter was used as the visible light source (400 nm ~ 700 nm), and was positioned 10 cm away from the photoelectrochemical cell. Transient photocurrent density measurement was performed in 0.01 M Na₂S electrolyte solution using a 20 son-off ; cycle

at a bias voltage of 0.7 V.

2.9. The apparent quantum efficiency (AQE) measurement

A 300-W Xe arc lamp was used as the light source for photocatalytic reaction. The measurement of AQE was performed using the same amount of reactants except for different laser irradiation for 3 h. We controlled the reaction time within 3 h because of only mono-substituted product in the initial stage of reaction. Various light filters were used to control the wavelength regions of irradiation light. We fixed the wavelength at 300 nm < λ < 400 nm for UV irradiation, 400 nm < λ < 700 nm for Vis irradiation, and 780 nm < λ < 1500 nm for NIR irradiation. The laser power in the photocatalytic reaction was collected using a power meter (Newport; 843-R). The corresponding wavelength captured for AQE calculation is located at 300 ± 10 nm, 450 ± 10 nm, and 900 ± 10 nm. Thus, the AQE was calculated as the following equation, AQE = n/n_p × 100%, in which n and n_p were denoted as the molecular number of generated mono-substituted product and the number of incident photons in 3 h, respectively.

2.10. The calculation of apparent quantum efficiency (AQE)

Under visible light irradiation (450 ± 10 nm), the catalytic suspension was irradiated by a 300 W Xe lamp equipped with 450 ± 10 nm band-pass filter for 3 h. During the reaction, only mono-substituted product was generated in the initial stage of reaction, which is reasonable for parallel calculation. The average intensity of irradiation was determined to be 0.263 W and 0.219 W before and after the reaction flask by a power meter (Newport; 843-R). So, total absorb light energy ΔE = (0.263–0.219) × 3 × 3600 = 475.2 J, initial mono-substituted product within 3 h, n = 20% × 0.5 mmol = 0.1 mmol, energy per photon E_0 = hc/λ = 6.63 × 10⁻³⁴ × 3 × 10⁸/(450 × 10⁻⁹) = 4.42 × 10⁻¹⁹ J, molar of photons n_p = ΔE/(E_0 × N_A) = 475.2/(4.42 × 10⁻¹⁹ × 6.02 × 10²³) = 1.786 × 10⁻³ mol = 1.786 mmol, $AQE_{(initial)}$ = n/n_p = 0.1/1.786 × 100% = 5.6%, were caculated. With the same method, we can calculate the initial AQE 4.3% and 4.5% for UV light irradiation (300 ± 10 nm) and NIR light irradiation (900 ± 10 nm), respectively.

2.11. Computational detail

We used Gaussian 16 A03 program [47] to study the reaction path. The intrinsic mechanism of the catalytic process is studied through searching the transition state of the electrons or holes injection and persuing the wave function analysis. All of transition state structure optimizations and the intrinsic reaction coordinate calculations were completed using B3LYP [48] functional and Def2-TZVP [49] basis set calculations. Accurate energy calculations were performed using ORCA-4.0.1.2 [50] combined with PWPB95-D3 [51,52] functional and Def2-QZVPP basis set. Topology analysis [53], ELF isosurface analysis were done using Multiwfn 3.5 program [54].

3. Results and discussion

3.1. Characterization results of Pd@MoS₂CPFs

The typical synthesis route leading to the Pd@MoS₂PFs was shown schematically in Scheme 1. MoS₂ NSs were obtained by chemical exfoliation method with commercial MoS₂ powder, and then react with α-thioctic acid (LA) to obtain MoS₂-LA NSs, which is easier to disperse in acetonitrile [55]. A fixed amount of MoS₂-LA colloidal solution was mixed with a certain amount of Py and Pd(OAc)₂, and then the above mixing solution was sonicated at room temperature for 1 h to obtain 3D Pd@MoS₂PFs. Due to the coordination between molybdenum atoms of MoS₂ and nitrogen atoms of PPy in one-step redox/complexation
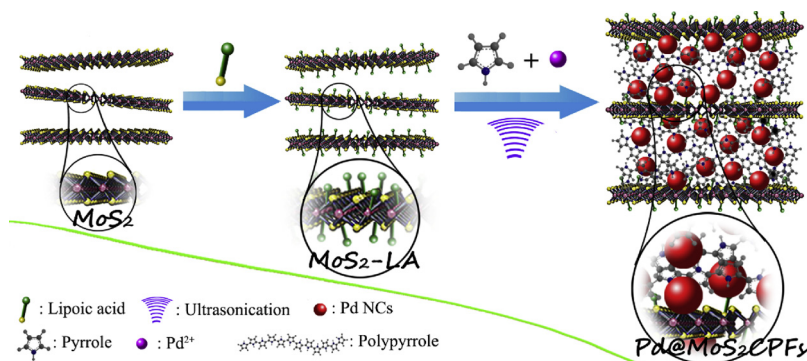
Scheme 1. Synthetic route and proposed formation mechanism of Pd@MoS$_2$CPFs.

process, exclusive and homogeneous polymerization on the 2D MoS$_2$ surfaces occurred to generate the porous 3D framework nanocomposites. Meanwhile, the Pd NPs were *in-situ* generated and encapsulated in the porous of MoS$_2$CPFs networks.

The morphology and hierarchical porous structure of 3D Pd@MoS$_2$CPFs nanohybrids were investigated by scanning electric microscope (SEM). The Pd@MoS$_2$CPFs hybrids exhibited unique interconnected hierarchical porous structures (Fig. 1b and c). However, no pores are visible in the MoS$_2$-LA (Fig. S1a). These pores were formed by the cross-link covalence and coordination among MoS$_2$ NSs, PPy and Pd NPs. Also, the independent Pd@CPFs microspheres (Fig. 1a and Fig. S2) were not found in the 3D Pd@MoS$_2$CPFs, indicating the complete integration among the ternary hybrids. The microstructures were further studied by TEM and HRTEM image. Figure S1b shows that MoS$_2$-LA exhibited transparent sheets. After the formation of 3D Pd@MoS$_2$CPFs hybrids, a very dense MoS$_2$ layer was appeared (Fig. 1d), confirming that the formed Pd@CPFs were embedded between two sheets of MoS$_2$. Notably, monodispersed Pd NPs were densely distributed and homogeneously embedded in MoS$_2$CPFs matrix, and the aggregation of particles was not observed. The diameter of Pd NPs is uniform with the mean size at 2.5 nm. In addition, the HRTEM image (Fig. 1e) disclosed that the spherical Pd NPs showed resolved lattice fringes at *d*-spacing of 0.234 nm, which could be indexed as Pd (111) planes [56]. The Pd@MoS$_2$CPFs hybrids contain Mo, Pd, C, N, S, and O elements, shown in Fig. 1f. Pd, Mo, S, C, N, and O elements are uniformly dispersed in the 3D Pd@MoS$_2$CPFs hybrids (Fig. 1g∼o). In contrast to C, S, N, O, and Mo signals, the Pd signals are confined in the nano-sized regions, revealing the *in-situ* generated Pd NPs are in uniform nanosize (Fig. 1n, o). In addition, from the ICP-AES analysis, the palladium load in Pd@MoS$_2$CPFs is only 13.1 wt%. Pd@MoS$_2$CPFs hybrids were further confirmed by XPS (Figs. S4, S5), BET (Fig. S6a, b), Raman spectrum (Fig. S6c, d), XRD (Fig. S6e), and TGA (Fig. S6f). For a complete understanding of the formation process of the Pd@MoS$_2$CPFs hybrids, we explored the amount influence of PPy and Pd(OAc)$_2$ on the morphonogy of formed Pd@MoS$_2$CPFs hybrids. (Fig. S7)

The UV − vis-NIR diffuse reflectance spectra of Pd@MoS$_2$CPFs, MoS$_2$ NSs, MoS$_2$CPFs, and PPy were compared in Fig. 2a. The absorption edge of solitary MoS$_2$ is located at 600 nm, and the energy band gap (Eg) is calculated to be 2.11 eV [57]. The PPy sample clearly showed the absorbance band at around 480 nm and 750 nm, attributed to the sum of the polarons and bipolarons [58]. For MoS$_2$CPFs, there is a strong absorption in the region from 900 to 1400 nm due to the formation of a doped, conducting form of PPy. After formation of Pd@MoS$_2$CPFs, the absorption band was enhanced in the 900∼1800 nm range, indicating strong charge interaction of the MoS$_2$ NSs, PPy, and Pd NPs. Therefore, the light harvesting efficiency of the Pd@MoS$_2$CPFs was higher than that of MoS$_2$CPFs in the NIR light region, which is beneficial for the photocatalytic activity. Fig. 2b summarizes the electron paramagnetic resonance (EPR) spectra recorded at room temperature for MoS$_2$, Pd@CPFs, MoS$_2$CPFs and Pd@MoS$_2$CPFs. In general,

the EPR is sensitive to paramagnetic species such as oxidized PPy$^+$ and metal ions, while it is silent for neutral species [39,59]. It is nearly silent of the signal in pure MoS$_2$ even under light irradiation because of rapid e$^-$/h$^+$ pairs recombination. The concentration of the PPy$^+$ in MoS$_2$CPFs increases under irradiation, thus showing stronger signal. The similar trend of EPR spectra for Pd@CPFs revealed that there is a transfer of electrons from excited PPy (PPy$^+$) to Pd nanoparticles. In comparison with MoS$_2$, MoS$_2$CPFs and Pd@CPFs, the EPR signal of Pd@MoS$_2$CPFs showed the largest increase in signal intensity in dark and under light irradiation, which may also be caused by the plasmonic effects on the Pd NPs. It is inferred from the significantly most intense EPR signal that more long-lived e$^-$/h$^+$ pairs could be generated in Pd@MoS$_2$CPFs under light irradiation. As shown in Fig. 2c, compared with alone MoS$_2$CPFs, Pd@MoS$_2$CPFs exhibited stronger photocurrent response, confirming the charge-carrier separation of MoS$_2$CPFs by Pd NPs under visible irradiation.

Fig. 2d illustrated a schematic of energy band diagram of the Pd@MoS$_2$CPFs. According to the Tauc plots (Fig. S8 as well as the detailed description in the Supporting Information) and cyclic voltammetry (Fig. S9 as well as the detailed description in the Supporting Information) test, we estimated conduction, valence band edges, and Eg values of PPy and MoS$_2$ [60]. Among the three materials, the lowest unoccupied molecular orbital (LUMO) levels of the PPy is located the highest in the diagram, conduction band (CB) of MoS$_2$ next, and Fermi level of Pd the lowest. The Pd NPs served as electron sinks to receive the photogenerated electrons from the excited MoS$_2$-conjugated microporous polypyrrole networks. The above formation of synergism could help to quickly separate charge and effectively retard the recombination between photo-generated e$^-$/h$^+$ pairs, so as to enhance photocatalytic activity of Pd@MoS$_2$CPFs.

3.2. Direct Tsuji–Trost allylation of allylalcohol and 1,3-dicarbonyl

Given the unique porous features and enhanced visible and NIR absorption for Pd@MoS$_2$CPFs nanohybrids, we further evaluated the photocatalytic activity of this heterogeneous catalyst to direct allylation of 1,3-dicarbonyl with allylalcohol without activators under the visible light illumination at room temperature. In preliminary catalysis study, we use the allylalcohol **1** and ethyl acetoacetate **2** as model substrates for optimization of reaction conditions (Table 1). Among the different solvents tests (Table 1, entry 1∼16), the mixture solution of H$_2$O/EC (V/V = 2.0 mL/0.5 mL) is the best solvent (Table 1 entry 3). We screened various bases (Table 1, entry 1∼8), and found that Cs$_2$CO$_3$ gave the corresponding allylated products **3** in 98% yield (Table 1, entry 3). Meanwhile, the photocatalytic activities of MoS$_2$CPFs, Pd@CPFs, Pd@MoS$_2$, commercial Pd/C (Pd w%, 10%), and Pd@MoS$_2$CPFs without light for a comparison were also carried out. As shown in Fig. 3a, no traceable products were detected for MoS$_2$CPFs catalyst, suggesting that MoS$_2$CPFs is not active. Pd@MoS$_2$CPFs without light, Pd@CPFs, Pd@MoS$_2$, and commercial Pd/C only gave
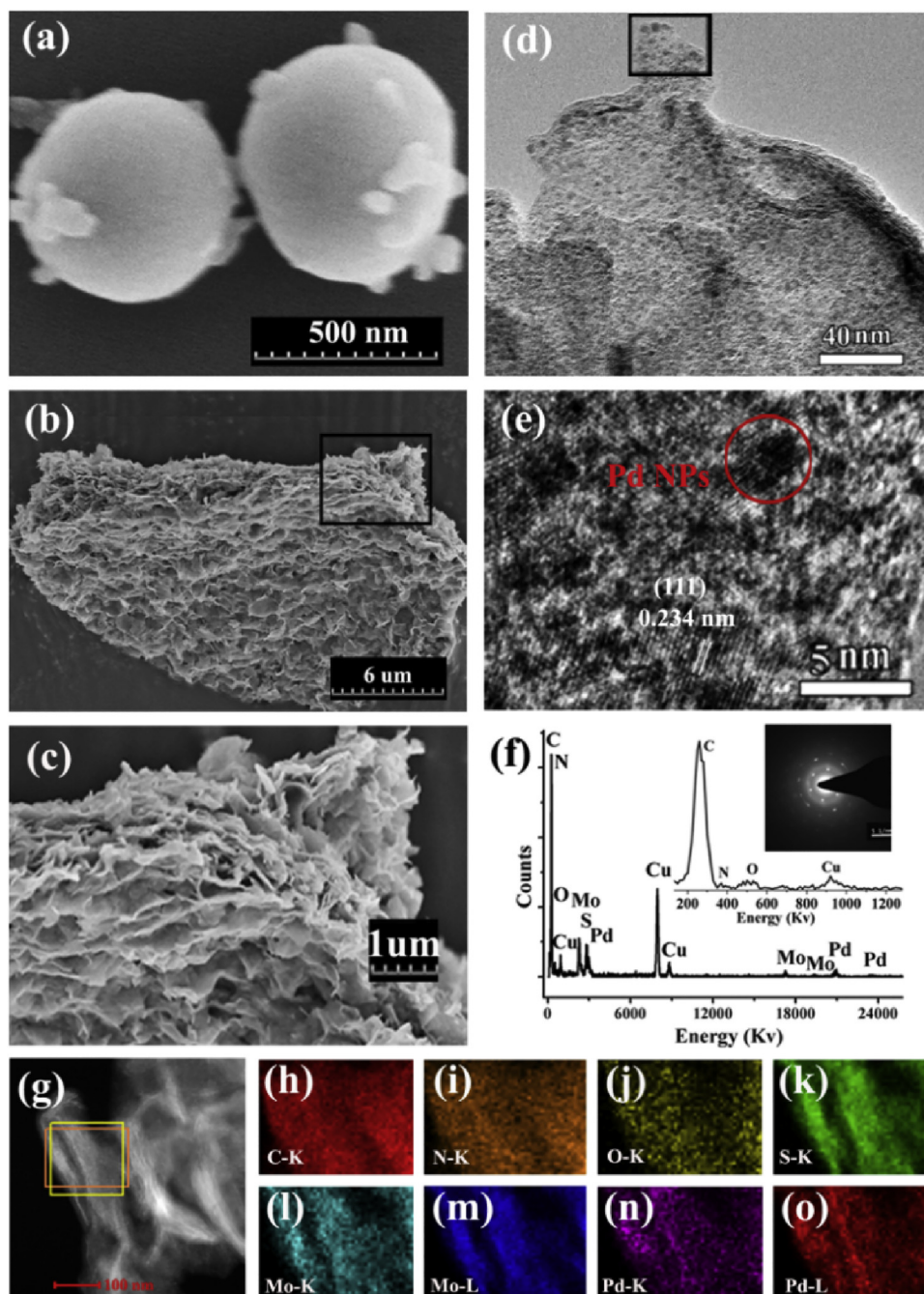
Fig. 1. SEM images of (a) Pd@CPFs and (b, c) 3D Pd@MoS$_2$CPFs nanohybrids. (d) TEM images and (e) corresponding HRTEM images of 3D Pd@MoS$_2$CPFs nanohybrids. (f) The typical EDX pattern and SAED pattern of 3D Pd@MoS$_2$CPFs nanohybrids. (g) HAADF image and the corresponding STEM-EDS elemental mapping images of carbon (h), nitrogen (i), oxide (j), sulfur (k), molybdenum (l, m) and palladium (n, o) in 3D Pd@MoS$_2$CPFs nanohybrids.

the low yields. However, only Pd@MoS$_2$CPFs catalyst showed the optimal photocatalytic activity. In addition, we found that the yields of Pd@MoS$_2$CPFs to direct allylation of 1,3-dicarbonyl with allylalcohol are great different at 25 °C using a thermostatic control device under different irradiation wavelength (Fig. 3b). In order to compare the apparent quantum efficiency (AQE) under different irradiation wavelength, we controlled the reaction time within 3 h because of only mono-substituted product in the initial stage of reaction. The highest yield in 400–700 nm indicates that the visible light contributed to the reaction mostly. The initial AQE achieves 5.6% at the wavelength of 450 ± 10 nm, while only 4.5% and 4.3% at the wavelength of 900 ± 10 nm and 300 ± 10 nm, indicating the Pd@MoS$_2$CPFs sample was active under visible-light irradiation. All these observations

collectively confirmed the presence of photoelectron transfer in those Tsuji-Trost reactions. Compared to other catalysts, the superiority activity of Pd@MoS$_2$CPFs can be attributed to the synergistic effect of MoS$_2$, PPy, and Pd in this Pd@MoS$_2$CPFs nanohybrids system. Furthermore, hierarchical pores structure helped to improve the contact area of the catalyst and substrate and catalyst, which is helpful to improve the catalytic yield.

Subsequently, we explored the 1,3-dicarbonyl substrate scope of the Pd@MoS$_2$CPFs catalytic allylation. Gratifyingly, as shown in Table 2, most of the substrates could be activated by the 3D Pd@MoS$_2$CPFs catalyst and show high yields. Notably, 97% yield was obtained for ethyl-2-methyl-3-oxobutanoate with steric bulk (Table 2, entries 1 g). The Pd@MoS$_2$CPFs catalyst also has good reaction activity for 1,3-
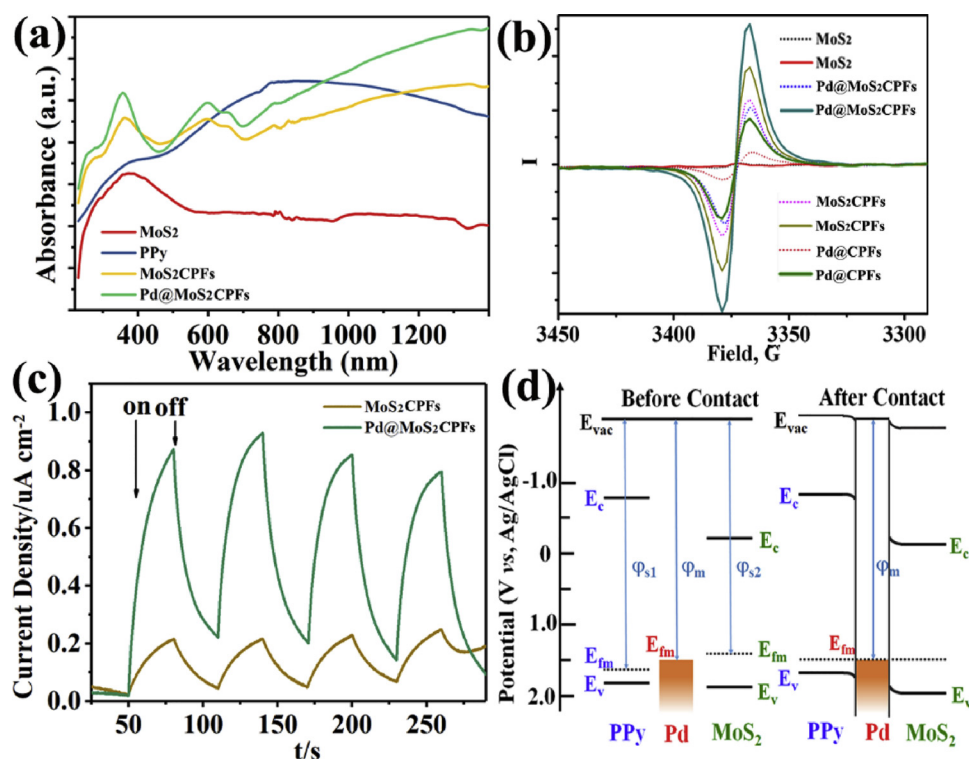
Fig. 2. (a) UV–vis–NIR diffuse reflectance spectra (UV–vis–NIR DRS) of MoS_2, PPy, MoS_2CPFs, and Pd@MoS_2CPFs. (b) Electron paramagnetic resonance (EPR) spectra of MoS_2, Pd@CPFs, MoS_2CPFs and Pd@MoS_2CPFs in dark (dash line) and under light irradiation (solid line). (c) Transient photocurrent density versus time plotted in 0.01 M Na_2S electrolyte under 400 nm ~ 700 nm. (d) Energy band diagram of the Mott–Schottky–type Pd@MoS_2CPFs contact system.

diester (Table 2, entries 1i and 1 j). When allyl ethyl carbonate replaced allylalcohol to react with ethyl acetoacetate, > 99% yields was obtained (Table 2, entries 1k). Moreover, Pd@MoS_2CPFs could achieve good to high yields for all 1,3-dicarbonyls under photoactivation, which is better compared to other reported nanocomposite under high temperature conditions [61].

3.3. Robust test and recycling of the Catalyst

High cycle stability is an inevitable topic of photocatalyst in green system, especially containing noble metal species. Reaction between allylalcohol **1** and ethyl acetoacetate **2** was performed to investigate the recycling behavior using the recovered catalyst. During each cycle, almost the same yield was generated, and no significant decay in the photocatalytic activity was observed in five successive cycles of our investigation (Fig. 4a), indicating that the Pd@MoS_2CPFs were stable and effective to direct allylation of 1,3-dicarbonyl with allylalcohol. In addition, after five successive cycles, only 0.67% of palladium was lost in the reaction solution. Meanwhile, the TEM and SEM imagies results of the used catalyst show little change in morphology or aggregation of the Pd@MoS_2CPFs nanohybrids and Pd NPs (Fig. 4b, c and Fig. S10). The high stability can be attributed to the confinement for Pd NPs and the coordination between Pd NPs and nitrogen in the matrices, restraining the fusion and migration of Pd NPs, and robust Schottky contact between Pd NPs and MoS_2.
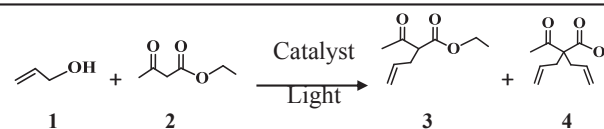
3.4. Mechanistic studies

In order to prove above synergistic effect, the Tsuji-Trost reaction between allylalcohol **1** and ethyl acetoacetate **2** in the presence of diisopropylethylamine (DIPEA) as a hole scavenger and benzoquinone (BQ) as a electron scavenger were performed [39,62]. As shown in Table 3, under the optimal condition without scavenger, 0.49 mmol (98%) yield was obtained. By adding DIPEA to block the hole, only 0.32 mmol (64%) yield was obtained, and 0.16 mmol (32%) ethyl acetoacetate **2** was detected. Via addition of BQ to block the electron, we got 0.15 mmol (30%) yield, and 0.3 mmol (60%) ethyl acetoacetate

2 was left. By blocking both hole and electron upon addition of both scavengers, only 0.09 mmol (18%) yield was obtained, and the 0.37 mmol (74%) ethyl acetoacetate **2** was collected. The different catalytic yield and different residual amount of ethyl acetoacetate **2** indicate that the generated e^-/h^+ pair plays a dominant role in the light-induced Tsuji-Trost allylation reaction. Upon irradiation, the photogenerated electron can attack 1,3-dicarbonyls, leading to the leaving of live hydrogen (Fig. 5), which was confirmed by high residual amount of ethyl acetoacetate in the presence of radical scavenger, and low residual amount of ethyl acetoacetate in the presence of hole scavenger. In addition, some studies have proved that the proton of ethyl acetoacetate was easily attacked by electron to form activated ketoester [63]. However, slightly lower yield was obtained when the hole scavenger was added, indicating that the hole plays an important role to activate the allylalcohol to form the π-allylpalladium species.

The intrinsic mechanism of the catalytic process was studied through searching the transition state of electrons or holes injection and pursuing the wave function analysis [47–49]. In Fig. 6a, the distance between the oxygen atom and the carbon atom reduced from 3.19 Å to 3.16 Å after holes injection in dehydroxylation transition state for allylalcohol. Holes injection behavior showed little effect on structural parameters of transition state1 (TS1). After dehydroxylation reaction was completed, η³-allylpalladium species was formed. The coupling reaction is divided into two parts: hydrogen transfer reaction of 1,3-dicarbonyl compound (TS2, TS4), and coupling of 1-propenyl and 1,3-dicarbonyl compound (TS3, TS5). For the hydrogen transfer reaction, hydrogen atom will not move from carbon atom to palladium atom along a straight line when no electrons are injected (the dot line in Fig. 6a). However, hydrogen atom will move close to palladium atom along a straight line when electrons are injected, resulting in much easier reaction. For the coupling reaction, the structure of TS3 showed little difference before and after electrons injection. Nevertheless, the distance between two terminal carbon atoms which contribute to the coupling reaction decreased from 2.27 Å to 1.85 Å after electrons injection (for TS5 from 2.18 Å to 1.89 Å). This shorter distance would consequently facilitate the coupling reaction.

In order to analyze the electronic structure of the dehydroxylation

Table 1
Tsuji-Trost reaction using Pd@MoS₂CPFs as photocatalyst.

Entry	Solvent	Base	3:4(%)[e]	Yield(%)[d]
1	H₂O	Cs₂CO₃	-	-
2	H₂O	-	-	-
3[b]	H₂O	Cs₂CO₃	20:80	98
4[bc]	H₂O	Cs₂CO₃	90:10	36
5[b]	H₂O	Li₂CO₃	90:10	38
6[b]	H₂O	Na₂CO₃	100:0	40
7[b]	H₂O	K₂CO₃	70:30	70
8[b]	H₂O	PPh₃	-	-
9	EtOH	Cs₂CO₃	-	-
10[b]	EtOH	Cs₂CO₃	100:0	55
11	THF	Cs₂CO₃	-	-
12[b]	THF	Cs₂CO₃	100:0	50
13	DMSO	Cs₂CO₃	-	-
14[b]	DMSO	Cs₂CO₃	100:0	60
15	DMF	Cs₂CO₃	-	-
16[b]	DMF	Cs₂CO₃	20:80	73

[a] **Reaction condition**: Pd@MoS₂CPFs (4 mg, Pd 5 umol), base (0.5 mmol)), **1** (100 uL, 1.5 mmol), **2** (65 uL, 0.5 mmol), solvent (2.0 mL), N₂, light, r.t., 20 h. [b] 0.5 mL of EC was added. [c] dark, r.t.. [d] Yields of isolated products.

Entry	Solvent	Base	3:4(%)[e]	Yield(%)[d]
1	H₂O	Cs₂CO₃	–	–
2	H₂O	–	–	–
3[b]	H₂O	Cs₂CO₃	20:80	98
4[bc]	H₂O	Cs₂CO₃	90:10	36
5[b]	H₂O	Li₂CO₃	90:10	38
6[b]	H₂O	Na₂CO₃	100:0	40
7[b]	H₂O	K₂CO₃	70:30	70
8[b]	H₂O	PPh₃	–	–
9	EtOH	Cs₂CO₃	–	–
10[b]	EtOH	Cs₂CO₃	100:0	55
11	THF	Cs₂CO₃	–	–
12[b]	THF	Cs₂CO₃	100:0	50
13	DMSO	Cs₂CO₃	–	–
14[b]	DMSO	Cs₂CO₃	100:0	60
15	DMF	Cs₂CO₃	–	–
16[b]	DMF	Cs₂CO₃	20:80	73

[a] **Reaction condition**: Pd@MoS₂CPFs (4 mg, Pd 5 umol), base (0.5 mmol)), **1** (100 uL, 1.5 mmol), **2** (65 uL, 0.5 mmol), solvent (2.0 mL), N₂, light, r.t., 20 h. [b] 0.5 mL of EC was added. [c] dark, r.t. [d] Yields of isolated products.

reaction before and after holes injection, we compare six real-space function values of the bond critical point (BCP) between the oxygen atom of TS1 and carbon atom previously bonded to oxygen atom by applying the topology analysis method (Quantum theory of Atom in Molecular, QTAIM) (Fig. 6b) [53]. The electron density, Lagrangian kinetic energy density, and Laplacian electron density at BCP were used to characterize the bond strength [48–52]. After holes injection, these three values drastically decrease, indicating that the bond strength between the hydroxyl group and the 1-propenyl group has become weaker. This change contributes to the occurrence of the reaction. We used the isosurface of the ELF function (isovalue = 0.8) to dynamically

analyze the changes of the electronic structure [54]. It can be found that the bond between the hydroxyl group and the 1-propenyl group weakens after holes injection, which will facilitate the dihydroxylation reaction (Animation 1 and Animation 2, the cylindrical isosurface between the hydroxyl group and the 1-propene disappears after holes injection.).

The real-space function of TS2 in the hydrogen transfer reaction is similar to that of TS1 (Fig. 6c). The Laplacian value of the electron density after electrons injection decreases drastically, indicating that the bond strength weakens after electrons injection. This will facilitate the break of hydrogen and carbon bond. In addition, the electron
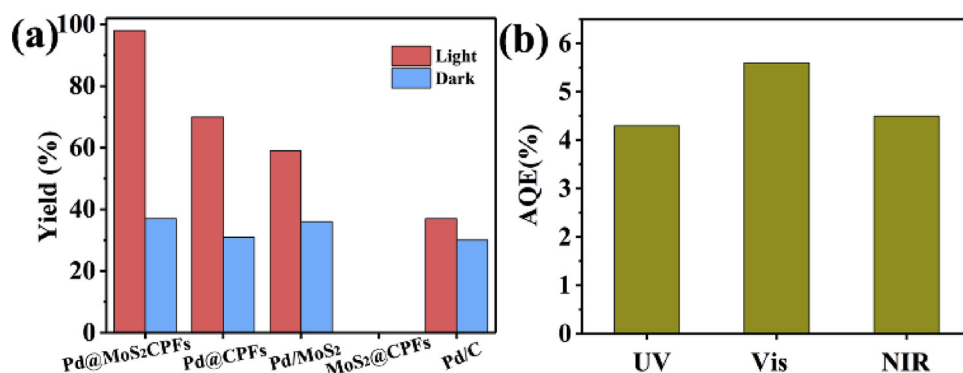
Fig. 3. (a) Comparison of photocatalytic allylation of ethyl acetoacetate 2 with allylalcohol 1 by different photocatalysts under white LED lamp irradiation and corresponding dark condition for 20 h at rt. (b) Initial photocatalytic yield and apparent quantum efficiency (AQE) of Pd@MoS$_2$CPFs for Tsuji–Trost reaction under different laser irradiation for 3 h at rt. The corresponding wavelength located at 300 ± 10 nm, 450 ± 10 nm, and 900 ± 10 nm.

density reduces from 0.13933 to 0.0088 a.u. after electrons injection. In the view of QTAIM theory, it is explained that the hydrogen and carbon bond does not belong to strong chemical bond interaction at this time, whereas it belongs to weak hydrogen bond domains.

For the coupling reaction (TS3), after electrons injection, the real-space function of BCP between carbon atoms at two ends of the coupling reaction changes significantly (Fig. 6d). Generally, the interaction can be considered as the electrostatic interaction when the Laplacian value of the electron density is greater than 0, and the electron density ranges from 0.03 to 0.1 a.u. Based on QTAIM, the resultant electron density is greater than 0.1 a.u. and both the electron density and Laplacian value of the electrondensity are less than 0 a.u, indicating that the transition state of the coupling reaction (TS3) has changed from the ionic interaction to the covalent interaction after electrons injection. Similarly, the same coupling reaction is also applicable for TS5. In the transition states TS3 and TS5 of the coupling reaction, due to photo-induced excitation, there are already features of covalent bonds between two ends of the coupling reaction after electron injection

(compared to the case without electron injection). This conclusion can be drawn from Fig. S11 and Fig. S12. These two graphs are the electron density Laplacian projection isosurface plots of the planes where the two endpoint carbon atoms of the coupling reaction are located. In these two plots, the red regions represent covalent interactions. It is clear that there are no covalent interactions between two transitional structures before the electron injection (Fig. S11a and Fig. S12a). However, there is a clear covalent interaction between the two carbon atoms after the electron injection (Fig. S11b and Fig. S12b), which is favorable for the reaction.

4. Conclusion

In summary, we have shown the first synthesis of a Pd@MoS$_2$CPFs by ultrasound mediated one-step redox/complexation process, in which the ultrafine Pd NPs are well dispersed throughout the material and show excellent size control within the pore matrix. In such structure, the Pd NPs/MoS$_2$ and Pd NPs/PPy formed close Schottky contact. The

Table 2
Scope of the photocatalytic Tsuji-Trost reaction with various substituents using Pd@MoS$_2$CPFs as photocatalyst.

2a, 24 h, Yield:>99%, **3:4** = 0:100

2b, 20 h, Yield: 98%, **3:4** = 20:80

2c, 24 h, Yield: 96%, **3:4** = 55:45

2d, 24 h, Yield: 93%, **3:4** = 90:10

2e, 24 h, Yield: 93%, **3:4** = 5:95

2f, 26 h, Yield: 90%, **3:4** = 40:60

2g, 9 h, Yield: 97%, **3:4** = 100:0

2h, 24 h, Yield: 97%, **3:4** = 0:100

2i, 50 h, Yield: 85%, **3:4** = 70:30

2j, 50 h, Yield: 89%, **3:4** = 60:40

2k, 20 h, Yield: >99%, **3:4** = 30:70

Reaction condition: Pd@MoS$_2$CPFs (4 mg, Pd 5 umol), Cs$_2$CO$_3$ (0.5 mmol)), **1** (100 uL, 1.5 mmol), **2** (65 uL, 0.5 mmol), H$_2$O/EC=2.0 mL/0.5 mL), N$_2$, r.t., Light source: White LED lamp, 30 W. Yields of isolated products and determined by ^{1}H-NMR and ^{13}C-NMR.
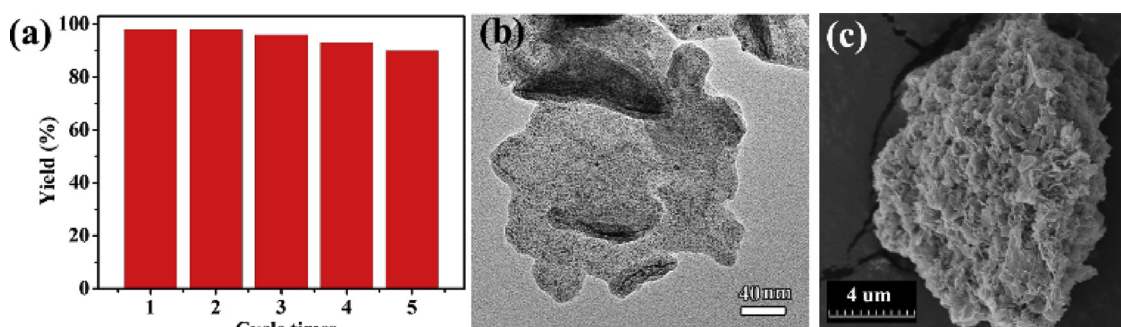
Fig. 4. Recycling abilities of Pd@MoS₂CPFs for Tsuji-Trost reaction under visible light irradiation. (b) TEM and (c) SEM images of Pd@MoS₂CPFs nanohybrids after reusing 5 times.

PPy not only stabilized Pd NPs but also directly/indirectly injected the photogenerated electrons into Pd NPs. Furthermore, the MoS₂ nanosheets also injected the photogenerated electrons into Pd NPs. Therefore, such frameworks help to synergistically promote the charge transfer abilities and retard the recombination of e^-/h^+ pairs of MoS₂CPFs. Benefit from above features, Pd@MoS₂CPFs catalyst firstly realized the photocatalytic direct Tsuji-Trost reaction between allylalcohol and 1,3-dicarbonyl at room temperature under visible light irradiation. The Pd catalyzed Tsuji–Trost reaction was accelerated by MoS₂CPFs and Pd NPs. The synergistic catalysis was observed only when the Pd NPs and MoS₂CPFs formed Mott–Schottky junction. The above experiments were further confirmed through searching the transition state of electrons or holes injection and pursuing the wave function analysis. This work highlights the use of photo energy at room temperature and the direct allylation with allyacohol.
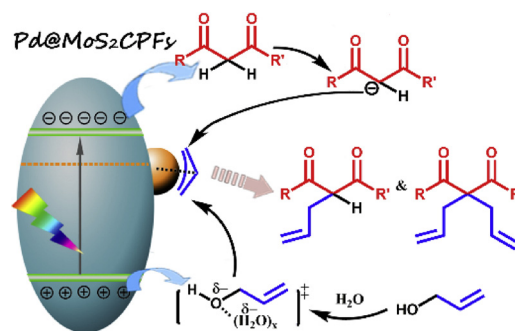

Fig. 5. Proposed reaction mechanism of the photocatalytic Tsuji-Trost reaction between allylalcohol and 1,3-dicarbonyl substrates with Pd@MoS₂CPFs.

Table 3
Comparison of photocatalytic allylation of 1,3-dicarbonyl substrate with allylalcohol by Pd@MoS₂CPFs photocatalyst under white LED lamp irradiation in absence or presence of scavenger.
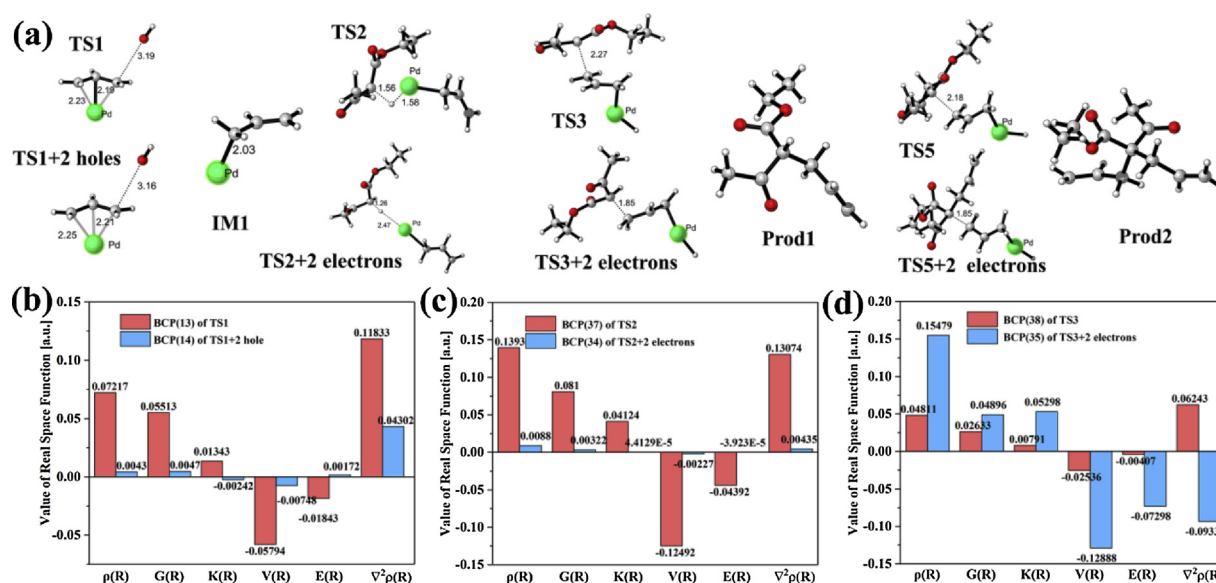

Entry	Condition	Light	3+4 (mmol)	Yield(%)[a]	2 (mmol)[b]
1	-	-	0.145	29	0.335
2	-	+	0.49	98	-
3	DIPEA	+	0.32	64	0.16
4	BQ	+	0.15	30	0.30
5	DIPEA+BQ	+	0.09	18	0.37

[a] **Reaction condition**: Pd@MoS₂CPFs (4 mg, Pd 5 umol), Cs₂CO₃ (0.5 mmol)), **1** (100 uL, 1.5 mmol), **2** (65 uL, 0.5 mmol), solvent (H₂O/EC=2.0 mL/0.5 mL), N₂, r.t., 20 h. [b] Retained substances.

Entry	Condition	Light	3 + 4 (mmol)	Yield(%)[a]	2 (mmol)[b]
1	–	–	0.145	29	0.335
2	–	+	0.49	98	–
3	DIPEA	+	0.32	64	0.16
4	BQ	+	0.15	30	0.30
5	DIPEA + BQ	+	0.09	18	0.37

[a] **Reaction condition**: Pd@MoS₂CPFs (4 mg, Pd 5 umol), Cs₂CO₃ (0.5 mmol)), **1** (100 uL, 1.5 mmol), **2** (65 uL, 0.5 mmol), solvent (H₂O/EC = 2.0 mL/0.5 mL), N₂, r.t., 20 h.
[b] Retained substances.

Fig. 6. (a) Reaction mechanism diagram with electron and hole injection. (b ~ d) Six real space function values for the critical point of TS1, TS2 and TS3, respectively. $\rho(R)$, $\nabla^2\rho(R)$, $G(R)$, $K(R)$, $V(R)$, and $E(R)$ are the density of all electrons, Laplacian of density of all electrons, Lagrangian kinetic energy, Hamiltonian kinetic energy, potential energy, and energy density, respectively.

Appendix A. Supplementary data

Supplementary material related to this article can be found, in the online version, at doi:https://doi.org/10.1016/j.apcatb.2018.11.030.

References

[1] X. Chang, T. Wang, P. Zhang, J. Zhang, A. Li, J. Gong, Enhanced surface reaction kinetics and charge separation of p–n heterojunction Co_3O_4/$BiVO_4$ photoanodes, J. Am. Chem. Soc. 137 (2015) 8356–8359.

[2] J. Li, S.K. Cushing, P. Zheng, T. Senty, F. Meng, A.D. Bristow, A. Manivannan, N. Wu, Solar hydrogen generation by a CdS-Au-TiO_2 sandwich nanorod array enhanced with Au nanoparticle as electron relay and plasmonic photosensitizer, J. Am. Chem. Soc. 136 (2014) 8438–8449.

[3] T. Wang, Z. Luo, C. Li, J. Gong, Controllable fabrication of nanostructured materials for photoelectrochemical water splitting via atomic layer deposition, Chem. Soc. Rev. 43 (2014) 7469–7484.

[4] F.E. Osterloh, Inorganic nanostructures for photoelectrochemical and photo-catalytic water splitting, Chem. Soc. Rev. 42 (2013) 2294–2320.

[5] N. Zhang, X.Y. Li, H.C. Ye, S.M. Chen, H.X. Ju, D.B. Liu, Y. Lin, W. Ye, C.M. Wang, Q. Xu, J.F. Zhu, L. Song, J. Jiang, Y.J. Xiong, Oxide defect engineering enables to couple solar energy into oxygen activation, J. Am. Chem. Soc. 136 (2016) 8928–8935.

[6] Y.D. Liu, A.W. Tang, Q. Zhang, Y.D. Yin, Seed-mediated growth of anatase TiO_2 nanocrystals with core–Antenna structures for enhanced photocatalytic activity, J. Am. Chem. Soc. 137 (2015) 11327–11339.

[7] D. Mills, Advances in solar thermal electricity technology, Sol. Energy 76 (2004) 19–31.

[8] B. Parida, S. Iniyan, R. Goic, A review of solar photovoltaic technologies, Renew. Sust. Energ. Rev. 15 (2011) 1625–1636.

[9] T.T. Chow, A review on photovoltaic/thermal hybrid solar technology, Acs Appl. Energy Mater. 87 (2010) 365–379.

[10] J. Cui, Y. Li, L. Liu, L. Chen, J. Xu, J. Ma, G. Fang, E. Zhu, H. Wu, L. Zhao, L. Wang, Y. Huang, Near-infrared plasmonic-enhanced solar energy harvest for highly efficient photocatalytic reactions, Nano Lett. 15 (2015) 6295–6301.

[11] S.I. Nikitenko, T. Chave, C. Cau, H.P. Brau, V. Flaud, Photothermal hydrogen production using noble-metal-Free Ti@TiO_2 core–Shell nanoparticles under visible–NIR light irradiation, ACS Catal. 5 (2015) 4790–4795.

[12] S. Naya, T. Niwa, R. Negishi, H. Kobayashi, H. Tada, Multi-electron oxygen reduction by a hybrid visible-light-Photocatalyst consisting of metal-oxide semi-conductor and self-assembled biomimetic complex, Angew. Chem. Int. Ed. 53 (2014) 13894–13897.

[13] F.Z. Su, S.C. Mathew, G. Lipner, X.Z. Fu, M. Antonietti, S. Blechert, X.C. Wang, Mpg-C_3N_4-Catalyzed selective oxidation of alcohols using O_2 and visible light, J. Am. Chem. Soc. 132 (2010) 16299–16301.

[14] Q. Xiang, J. Yu, M. Jaroniec, Synergetic effect of MoS_2 and graphene as cocatalysts for enhanced photocatalytic H_2 production activity of TiO_2 nanoparticles, J. Am. Chem. Soc. 134 (2012) 6575–6578.

[15] H. Zhu, X. Ke, X. Yang, S. Sarina, H. Liu, Reduction of nitroaromatic compounds on supported gold nanoparticles by visible and ultraviolet light, Angew. Chem. Int. Ed. 49 (2010) 9657–9661.

[16] A. Li, T. Wang, X. Chang, W. Cai, P. Zhang, J. Zhang, J. Gong, Spatial separation of oxidation and reduction co-catalysts for efficient charge separation: Pt@TiO_2@ MnO_x hollow spheres for photocatalytic reactions, Chem. Sci. 7 (2016) 890–895.

[17] M.A. Lukowski, A.S. Daniel, F. Meng, A. Forticaux, L. Li, S. Jin, Enhanced hydrogen evolution catalysis from chemically exfoliated metallic MoS_2 nanosheets, J. Am. Chem. Soc. 135 (2013) 10274–10277.

[18] A. Splendiani, L. Sun, Y. Zhang, T. Li, J. Kim, C.Y. Chim, G. Galli, F. Wang, Emerging photoluminescence in monolayer MoS_2, Nano Lett. 10 (2010) 1271–1275.

[19] X. Zong, H. Yan, G. Wu, G. Ma, F. Wen, L. Wang, C. Li, Enhancement of photo-catalytic H_2 evolution on CdS by loading MoS_2 as cocatalyst under visible light irradiation, J. Am. Chem. Soc. 130 (2008) 7176–7177.

[20] K. Chang, Z. Mei, T. Wang, Q. Kang, S. Ouyang, J. Ye, MoS_2/Graphene cocatalyst for efficient photocatalytic H_2 evolution under visible light irradiation, ACS Nano 8 (2014) 7078–7087.

[21] S. Bai, L. Wang, X. Chen, J. Du, Y. Xiong, Chemically exfoliated metallic MoS_2 nanosheets: a promising supporting co-catalyst for enhancing the photocatalytic performance of TiO_2 nanocrystals, Nano Res. 8 (2014) 175–183.

[22] Y. Hou, Z. Wen, S. Cui, X. Guo, J. Chen, Constructing 2D porous graphitic C_3N_4 Nanosheets/Nitrogen-doped Graphene/Layered MoS_2 ternary nanojunction with enhanced photoelectrochemical activity, Adv. Mater. 25 (2013) 6291–6297.

[23] Q. Li, N. Zhang, Y. Yang, G. Wang, D.H. Ng, High efficiency photocatalysis for pollutant degradation with MoS_2/C_3N_4 heterostructures, Langmuir 30 (2014) 8965–8972.

[24] Y. Shi, J. Wang, C. Wang, T.T. Zhai, W.J. Bao, J.J. Xu, X.H. Xia, H.Y. Chen, Hot Electron of Au nanorods activates the electrocatalysis of hydrogen evolution on MoS_2 nanosheets, J. Am. Chem. Soc. 137 (2015) 7365–7370.

[25] P.P. Wang, H. Sun, Y. Ji, W. Li, X. Wang, Three-dimensional assembly of single-layered MoS_2, Adv. Mater. 26 (2014) 964–969.

[26] L. Zhi, H. Zhang, Z. Yang, W. Liu, B. Wang, Interface coassembly of mesoporous MoS_2 based-frameworks for enhanced near-infrared light driven photocatalysis, Chem. Commun. 52 (2016) 6431–6434.

[27] L. Zhang, H.B. Wu, Y. Yan, X. Wang, X.W. Lou, Hierarchical MoS_2 microboxes constructed by nanosheets with enhanced electrochemical properties for lithium storage and water splitting, Energy Environ. Sci. 7 (2014) 3302–3306.

[28] S. Cho, M.J. Lee, M.S. Kim, S. Lee, Y.K. Kim, D.H. Lee, C.W. Lee, K.H. Cho, J.H. Chung, Infrared plus visible light and heat from natural sunlight participate in the expression of MMPs and type I procollagen as well as infiltration of in-flammatory cell in human skin in vivo, J. Dermatol. Sci. 50 (2008) 123–133.

[29] S. Ghosh, N.A. Kouame, L. Ramos, S. Remita, A. Dazzi, A. Deniset-Besseau, P. Beaunier, F. Goubard, P.H. Aubert, H. Remita, Conducting polymer

nanostructures for photocatalysis under visible light, Nat. Mater. 14 (2015) 505–511.

[30] X. Wang, K. Maeda, A. Thomas, K. Takanabe, G. Xin, J.M. Carlsson, K. Domen, M. Antonietti, A metal-free polymeric photocatalyst for hydrogen production from water under visible light, Nat. Mater. 8 (2009) 76–80.

[31] L. Zhang, P. Liu, Z. Su, Preparation of PANI–TiO₂ nanocomposites and their solid-phase photocatalytic degradation, Polym. Degrad. Stabil. 91 (2006) 2213–2219.

[32] D. Chowdhury, D. Paul, A. Chattopadhyay, Photocatalytic polypyrrole-TiO₂-nano-particles composite thin film generated at the air-water interface, Langmuir 21 (2005) 4123–4128.

[33] Y. Yang, J. Wen, J. Wei, R. Xiong, J. Shi, C. Pan, Polypyrrole-decorated Ag-TiO₂ nanofibers exhibiting enhanced photocatalytic activity under visible-light illumi-nation, ACS Appl. Mater. Inter. 5 (2013) 6201–6207.

[34] T.A. Kandiel, R. Dillert, D.W. Bahnemann, Enhanced photocatalytic production of molecular hydrogen on TiO₂ modified with Pt-polypyrrole nanocomposites, Photochem. Photobiol. Sci. 8 (2009) 683–690.

[35] N. Gaikwad, S. Bhanoth, P.V. More, G.H. Jain, P.K. Khanna, Chemically designed Pt/PPy nano-composite for effective LPG gas sensor, Nanoscale 6 (2014) 2746–2751.

[36] H. Tang, J. Wang, H. Yin, H. Zhao, D. Wang, Z. Tang, Growth of polypyrrole ul-trathin films on MoS₂ monolayers as high-performance supercapacitor electrodes, Adv. Mater. 27 (2015) 1117–1123.

[37] L. Wang, J. Schindle, J.A. Thomas, C.R. Kannewurf, M.G. Kanatzidis, Entrapment of polypyrrole chains between MoS₂ layers via an in situ oxidative polymerization encapsulation reaction, Chem. Mater. 7 (1995) 1753–1755.

[38] G. Ma, H. Peng, J. Mu, H. Huang, X. Zhou, Z. Lei, In situ intercalative poly-merization of pyrrole in graphene analogue of MoS₂ as advanced electrode material in supercapacitor, Power Sources 229 (2013) 72–78.

[39] Z.J. Wang, S. Ghasimi, K. Landfester, K.A.I. Zhang, Photocatalytic suzuki coupling reaction using conjugated microporous polymer with immobilized palladium na-noparticles under visible light, Chem. Mater. 27 (2015) 1921–1924.

[40] B. Wu, D. Liu, S. Mubeen, T.T. Chuong, M. Moskovits, G.D. Stucky, Anisotropic growth of TiO₂ onto gold nanorods for plasmon-enhanced hydrogen production from water reduction, J. Am. Chem. Soc. 138 (2016) 1114–1117.

[41] P. Christopher, H. Xin, S. Linic, Visible-light-enhanced catalytic oxidation reactions on plasmonic silver nanostructures, Nat. Chem. 3 (2011) 467–472.

[42] S.T. Kochuveedu, Y.H. Jang, D.H. Kim, A study on the mechanism for the interac-tion of light with noble metal-metal oxide semiconductor nanostructures for various photophysical applications, Chem. Soc. Rev. 42 (2013) 8467–8493.

[43] B.M. Trost, M.L. Crawley, Asymmetric transition-metal-catalyzed allylic alkylations: applications in total synthesis, Chem. Rev. 103 (2003) 2921–2943.

[44] M. Wakizaka, T. Matsumoto, R. Tanaka, H. Chang, Dehydrogenation of anhydrous methanol at room temperature by o-aminophenol-based photocatalysts, Nat. Commun. 7 (2016) 12333–12344.

[45] P. Joensen, R.F. Frindt, S.R. Morrison, Single-layer MoS₂, Mater. Res. Bull. 21 (1986) 457–461.

[46] D.A. Shirley, Theory of KLL auger energies including static relaxation, Phys. Rev. A 7 (1973) 1520–1528.

[47] M. Frisch, G. Trucks, H. Schlegel, G. Scuseria, M. Robb, J. Cheeseman, G. Scalmani, V. Barone, G. Petersson, H. Nakatsuji, Wallingford CT. 2016.

[48] A.D. Becke, Density-functional exchange-energy approximation with correct asymptotic behavior, Phys. Rev A 38 (1988) 3098–3100.

[49] F. Weigend, R. Ahlrichs, Balanced basis sets of split valence, triple zeta valence and quadruple zeta valence quality for H to Rn: design and assessment of accuracy, Phys. Chem. Chem. Phys. 7 (2005) 3297–3305.

[50] F. Neese, Wiley Interdisciplinary Reviews: Computational Molecular Science vol 2, (2012), pp. 73–78.

[51] S. Grimme, J. Antony, S. Ehrlich, H. Krieg, A consistent and accurate ab initio parametrization of density functional dispersion correction (DFT-D) for the 94 elements H-Pu, J. Chem. Phys. 132 (2010) 154104.

[52] A. Karton, A. Tarnopolsky, J.F. Lamére, G.C. Schatz, J.M. Martin, Highly accurate first-principles benchmark data sets for the parametrization and validation of density functional and other approximate methods. Derivation of a robust, gen-erally applicable, double-hybrid functional for thermochemistry and thermo-chemical kinetics, J. Phys. Chem. A 112 (2008) 12868–12886.

[53] R.F. Bader, Encyclopedia of Computational Chemistry vol. 1, (2002).

[54] T. Lu, F.W. Chen, Multiwfn: a multifunctional wavefunction analyzer, J. Comput. Chem. 33 (2012) 580–592.

[55] S.S. Chou, M. De, J. Kim, S. Byun, C. Dykstra, J. Yu, J. Huang, V.P. Dravid, Ligand conjugation of chemically exfoliated MoS₂, J. Am. Chem. Soc. 135 (2013) 4584–4587.

[56] X. Xu, Y. Li, Y. Gong, P. Zhang, H. Li, Y. Wang, Synthesis of palladium nanoparticles supported on mesoporous N-doped carbon and their catalytic ability for biofuel upgrade, J. Am. Chem. Soc. 134 (2012) 16987–16990.

[57] N. Singh, G. Jabbour, U. Schwingenschlögl, Optical and photocatalytic properties of two-dimensional MoS₂, Eur. Phys. J. B 85 (2012) 392–395.

[58] F. Li, M.A. Winnik, A. Matvienko, A. Mandelis, Polypyrrole nanoparticles as a thermal transducer of NIR radiation in hot-melt adhesives, J. Mater. Chem. 17 (2007) 4309.

[59] N.M. Dimitrijevic, S. Tepavcevic, Y. Liu, T. Rajh, S.C. Silver, D.M. Tiede, Nanostructured TiO₂/Polypyrrole for visible light photocatalysis, J. Phys. Chem. C 117 (2013) 15540–15544.

[60] L.F. Gao, T. Wen, J.Y. Xu, X.P. Zhai, M. Zhao, G.W. Hu, P. Chen, Q. Wang, H.L. Zhang, Iron-doped carbon nitride-type polymers as homogeneous organoca-talysts for visible light-driven hydrogen evolution, ACS Appl. Mater. Inter. 8 (2016) 617–624.

[61] M. Yasuda, T. Somyo, A. Baba, Direct carbon–carbon bond formation from alcohols and active methylenes, alkoxyketones, or indoles catalyzed by indium trichloride, Angew. Chemie Int. Ed. English 45 (2006) 793–796.

[62] K.E. Knowles, M. Malicki, E.A. Weiss, Dual-time scale photoinduced Electron transfer from PbS quantum dots to a molecular acceptor, J. Am. Chem. Soc. 134 (2012) 12470–12473.

[63] H. Noda, K. Motokura, A. Miyaji, T. Baba, Heterogeneous synergistic catalysis by a palladium complex and an amine on a silica surface for acceleration of the Tsuji–Trost reaction, Angew. Chem. Int. Ed. 51 (2012) 8017–8020.